ACS Catalysis

Research Article

pubs.acs.org/acscatalysis

Breaking the Correlation between Energy Costs and Kinetic Barriers in Hydrogen Evolution via a Cobalt Pyridine-Diimine-Dioxime Catalyst

Pengfei Huo,[‡] Christopher Uyeda,[§] Jason D. Goodpaster,[∥] Jonas C. Peters,* and Thomas F. Miller III*

Division of Chemistry and Chemical Engineering, California Institute of Technology, Pasadena, California 91125, United States

Supporting Information

ABSTRACT: A central challenge in the development of inorganic hydrogen evolution catalysts is to avoid deleterious coupling between the energetics of metal site reduction and the kinetics of metal hydride formation. In this work, we combine theoretical and experimental methods to investigate cobalt diimine-dioxime catalysts that show promise for achieving this aim by introducing an intramolecular proton shuttle via a pyridyl pendant group. Using over 200 coupled-cluster-level electronic structure calculations of the Co-based catalyst with a variety of pyridyl substituents, the energetic and kinetic barriers to hydrogen formation are investigated, revealing nearly complete decoupling of the energetics of Co reduction and the kinetics of intramolecular Co hydride formation. These calculations employ recently developed quantum embedding methods that allow for local regions of a molecule to be described using high-accuracy wavefunction methods (such as CCSD(T)), thus overcoming significant errors in the DFT-level description of transition-metal complexes. Experimental synthesis and cyclic voltammetry of the methyl-substituted form of the catalyst indicate that protonation of the pendant group leaves the Co reduction potential unchanged, which is consistent with the theoretical prediction that these catalysts can successfully decouple the electronic structures of the transition-metal and ligand-protonation sites. Additional computational analysis indicates that introduction of the pyridyl pendant group enhances the favorability of intramolecular proton shuttling in these catalysts by significantly reducing the energetic barrier for metal hydride formation relative to previously studied cobalt diimine-dioxime catalysts. These results demonstrate a promising proof of principle for achieving uncoupled and locally tunable intramolecular charge-transfer events in the context of homogeneous transition-metal catalysts.

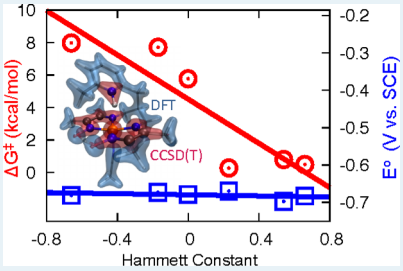

KEYWORDS: *hydrogen evolution, cobalt diimine-dioxime catalysts, proton shuttle, electrochemistry, coupled-cluster theory, density functional theory, embedding*

1. INTRODUCTION

The catalytic evolution of molecular hydrogen is a critical challenge in the efficient conversion and storage of solar energy.[1] Cobalt-based catalysts are promising model systems to study due to the earth abundance of cobalt, as well as the high stability, high Faradaic yield, and low overpotential that they can exhibit.[2−13] These complexes have been immobilized onto electrode surfaces[14−16] and incorporated into photochemical systems.[17−20] Particular focus in recent years has been given to hydrogen evolution via cobaloximes and other cobalt tetraaza macrocyclic catalysts.[8−10,21] Although the mechanism of these catalysts remains the focus of ongoing study,[22−24] their efficiency appears in many cases to depend upon both the thermodynamic potentials for catalyst reduction and the kinetics of the proton-transfer steps.[8,9,25] Specifically, Figure 1 illustrates two steps upon which the mechanism has been proposed to hinge, including an electron-transfer reaction that leads to the initial reduction of Co^{II} and establishes the primary external energetic cost for initiating hydrogen evolution (step A) and a proton-transfer reaction that leads to the formation of Co^{III} hydride (or an isomer thereof)[26] and creates the kinetic bottleneck in the catalytic cycle (step B).

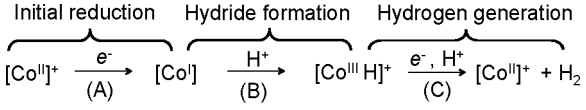

Figure 1. Standard mononuclear hydrogen evolution pathway.

Previous experimental and computational studies of cobalt dimethylglyoxime,[8,27] cobalt pentapyridine,[28] nickel diphosphine complexes,[29] and various other complexes[30,31] have found a severe "anti-correlation" between the reduction potential of step A and the rate associated with step B, such that modifications of the hydrogen-evolution catalysts that increase the reduction potential also have the effect of decreasing the rate of metal hydride formation. This anti-correlation arises because modification of the catalysts with electron-withdrawing groups diminishes the electron density on the metal center, simultaneously making it more easily reduced

Received: May 17, 2016
Revised: July 18, 2016
Published: July 26, 2016

DOI: 10.1021/acscatal.6b01387
ACS Catal. 2016, 6, 6114−6123

and more difficult to protonate;[27] it is a significant obstacle to the design of catalysts that evolve hydrogen with both a high rate and low overpotential.

DuBois and co-workers have proposed a promising strategy to decouple this anti-correlation in both nickel- and cobalt-based hydrogen evolution catalysts,[32,33] using multidentate phosphine ligands with a substituted amine group to provide an intramolecular proton shuttle, as illustrated in Figure 2. With

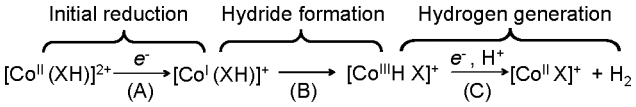

Figure 2. Hydrogen evolution pathway involving an intramolecular proton shuttle (X).

this system, partial decorrelation of the key reduction (A) and hydride formation (B) steps in Figure 2 has been observed, although strongly electron withdrawing substituent groups lead to the return of the anti-correlation between the energetics of the reduction potential and the kinetics of the metal hydride formation, presumably due to insufficient separation of the proton shuttle site and the redox center.

In this paper, we present a combined computational/experimental study that investigates an alternative molecular platform for eliminating the unwanted anti-correlation between the energetics of step A and the kinetics of step B in Figure 2. We focus on modification of the previously studied[21,34−36] cobalt diimine-dioxime catalyst (Figure 3, complex **1**). In

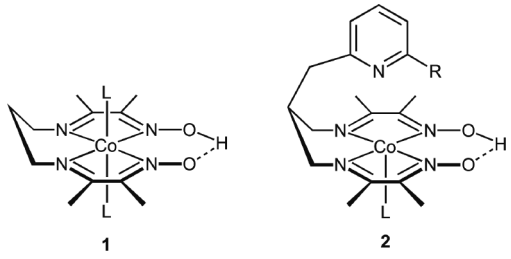

Figure 3. Cobalt diimine-dioxime catalysts, without (**1**) and with (**2**) the R-substituted pyridyl group.

particular, following earlier work[17,37] we investigate cobalt pyridine-diimine-dioxime complexes (Figure 3, complex **2**) that include a substituted pyridyl group to function as an intramolecular proton shuttle. In 1992, Marzilli reported the synthesis of the Co(CH$_2$pyr-dopnH) complex, which is analogous to complex **2** but lacking the 2-methyl substituent on the pyridine ring;[37] X-ray diffraction data on this complex indicated that the pyridine is bound to the Co center and is thus unlikely to be available to act as a proton shuttle. In an effort to disrupt the Co−pyridine interaction, we hypothesized that introduction of a 2-methyl substituent would cause steric frustration.

In addition to presenting the synthesis and characterization of the methyl-substituted (R = −CH$_3$) version of complex **2**, we employ a recently developed wavefunction-in-density functional theory (WF-in-DFT) embedding technique[38,39] to accurately compute the reduction potentials and reaction barriers associated with the key electron-transfer and proton-transfer steps in the catalyst with a range of different substituent groups. The calculations support the idea that the rate of metal hydride formation can be regulated independently of the reduction potential in a monometallic catalyst, illustrating a promising design principle for the efficient catalytic evolution of hydrogen.

2. COMPUTATIONAL AND EXPERIMENTAL METHODS

2.1. WF-in-DFT Embedding. Previous computational studies of cobalt-based hydrogen evolution catalysts have utilized DFT,[25,27,40] which can provide a useful compromise between accuracy and efficiency. However, numerous examples illustrate that DFT can be unreliable for the description of reaction barriers in transition-metal complexes.[41−45] In this work, we employ the recently developed projection-based WF-in-DFT embedding technique[38,39,46] to obtain accurate reaction barriers and reduction potentials associated with the key electron-transfer and proton-transfer steps for hydrogen evolution in the new class of cobalt pyridine-diimine-dioxime catalysts.

Projection-based WF-in-DFT embedding allows for a subset of the molecular system to be described at the level of a WF method, while the remainder of the system is treated at the level of DFT; this enables, for example, the region of the transition metal in the catalyst to be described using coupled cluster CCSD(T), while the surrounding ligands are treated using DFT. The method accounts for all interactions between subsystems at the DFT level, enabling an accurate description even for cases in which the subsystem partitioning spans across covalent bonds or a conjugated bonding pattern.[38,39] All WF-in-DFT calculations are performed using Molpro version 2012.1.[47]

For all WF-in-DFT calculations reported in this study, we employ CCSD(T) as the WF method, and we employ the B3P86 exchange-correlation functional for the DFT level of theory.[48−50] For open-shell systems, the WF method is unrestricted CCSD(T) (i.e., UCCSD(T)) on a restricted open-shell Hartree−Fock reference, as described in the Supporting Information. All embedding calculations employ a level shift parameter for the projection operator of 10^6 au, which was tested to be sufficiently large to ensure mutual orthogonality of the subsystem molecular orbitals.[38]

For the proton-transfer reactions, the embedding calculations employ the cc-pVTZ basis for all atoms,[51] except for the hydrogen atoms in the DFT region, which employ the cc-pVDZ basis;[51] the same basis set was used in the reference CCSD(T) calculations. For the redox reactions, which are significantly more computationally demanding due to the open-shell UCCSD(T) calculations, we employ the cc-pVTZ basis for the cobalt atom, while all other atoms employ the cc-pVDZ basis. To confirm that this smaller basis set was adequate, the Co$^{II/I}$ reduction potential for the fully protonated form of complex **1** was calculated using the larger cc-pVTZ basis for all atoms except hydrogen and this agreed with the smaller basis set results to within 0.05 V.

In projection-based WF-in-DFT embedding, the WF and DFT subsystems are defined by partitioning the occupied molecular orbitals (MOs) from a DFT calculation that is performed over the full system. To determine this partitioning in the current study, we first identify the atoms associated with the WF and DFT regions, using the protocol described below. Given this partitioning of the atoms between the WF and DFT regions, we then automatically determine the partitioning of the occupied MOs; specifically, the occupied MOs from the full DFT calculation are localized using the Pipek−Mezey algorithm,[52] and the MOs associated with the WF subsystem are identified to be those with a combined Mulliken population

DOI: 10.1021/acscatal.6b01387
ACS Catal. 2016, 6, 6114−6123

of at least 0.4 on the atoms of the WF region. The selection of the atoms for the WF region is performed as follows. For proton-transfer reactions considered in this study, the atoms associated with the WF region are illustrated in Figure 4B; the

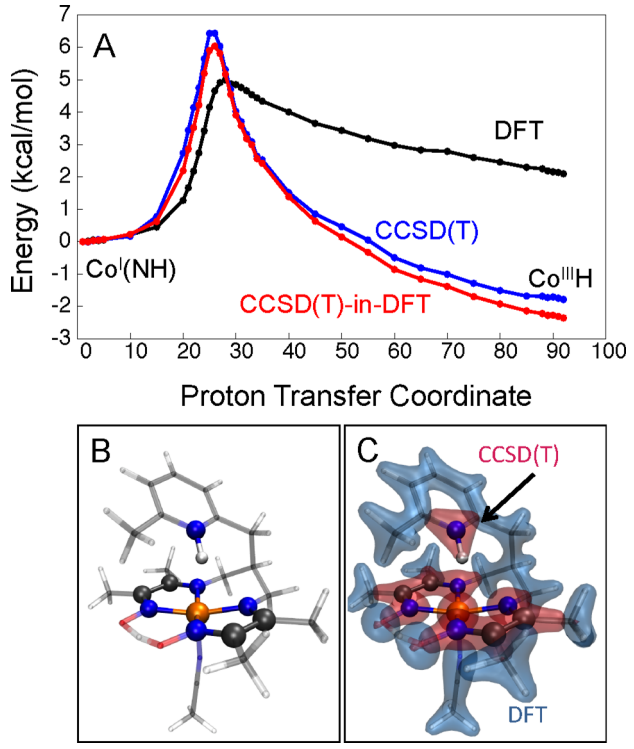

Figure 4. (A) Energy profiles for the intramolecular proton-transfer reaction in complex **2** with methyl substitution, obtained using CCSD(T) (blue), DFT (black), and CCSD(T)-in-DFT (red). (B) Partitioning of the system in the CCSD(T)-in-DFT calculations into atoms that are treated using CCSD(T) (solid ball−stick) and DFT (transparent stick). (C) Associated partitioning of the electronic density into subsystems that are treated using CCSD(T) (red) and DFT regions (blue).

same atoms are used irrespective of the substitution group on the pyridine ring. For the methyl-substituted system, convergence checks with respect to the size of the WF region were performed. In particular, by expanding the WF region to include the atoms of the acetonitrile, we find that the barrier and driving force changed by less than 0.3 kcal/mol; alternatively, by expanding the WF region to include the atoms of the pyridine ring and methyl group, we find that the barrier and driving force changed by less than 0.5 kcal/mol. Finally, Figure 4A demonstrates the excellent agreement between the results obtained with the partitioning shown in Figure 4B and CCSD(T) calculations performed over the full system, indicating convergence with respect to the size of the WF region. For the redox reactions on complex **2** that are performed in this study, it is found that the WF region was not yet converged using the partitioning illustrated in Figure 4B, and the results are thus reported using a larger WF region that are illustrated in Figure S7 in the Supporting Information. For the methyl-substituted system, convergence checks with respect to the size of the WF were performed. In particular, by expanding the WF region to include the atoms of the pyridine ring and methyl group, we find the reduction potential changed by less than 0.02 V. For the redox reactions on complex **1**, the WF region was defined exactly as in complex **2**, as illustrated in Figure S7.

To confirm that the multireference character of the cobalt-based compounds studied here is sufficiently small to enable reliable description with CCSD(T), the $\mathcal{T}1$ diagnostic was computed in all calculations; typically, CCSD(T) is considered accurate if the $\mathcal{T}1$ diagnostic is less than 0.02, although recent work suggests that a value of 0.05 is acceptable for 3d transition-metal species.[53] None of our closed-shell calculations had $\mathcal{T}1$ diagnostics larger than 0.009, and none of our open-shell calculations exceeded 0.044. Furthermore, we note that all calculations, even at near the transition-state regions, exhibit a HOMO−LUMO gap in excess of 4 eV, further suggesting that a single-reference approach such as CCSD(T) is sufficient.

To truncate the virtual space for both the reference CCSD(T) calculations and the WF-in-DFT calculations, we employ the local CCSD(T) method (i.e., LCCSD(T)) with orbital-specific virtuals.[54] LCCSD(T) methods have proven successful in previous applications to transition-metal catalysts.[55] The localized virtual orbitals are confirmed to reproduce the canonical pair energy of the diagonal pairs to within 10^{-4} Hartree. For reference calculations performed over the full system and for the WF-in-DFT calculations, the LCCSD(T) domains were consistently determined using the method of Boughton and Pulay[56] with a cutoff threshold of 0.999. For the embedding calculations, using this high value of the threshold ensures that all orbital pairs were correlated, with at least 80% at the CCSD(T) level and the remainder at the MP2 level; for the reference LCCSD(T) calculations performed over the full system, at least 35% of the pairs are correlated using CCSD(T), approximately 50% are correlated using using MP2, and the remainder of the pairs are uncorrelated. The high value of this threshold was found to be necessary to ensure that the LCCSD(T) calculations (including the reference LCCSD(T) calculations performed over the full system) exhibit smooth potential energy surfaces as a function of the nuclei positions. Furthermore, the LCCSD(T) calculations utilized density fitting (DF),[57] and the triples are approximated using the noniterative (T0) procedure.[58]

The WF-in-DFT calculations reported here exhibit up to 30-fold increases in speed with respect to LCCSD(T) performed over the entire system and considerably greater increases with respect to full CCSD(T) performed over the entire system. As the employment of LCCSD(T) in the embedding calculations is primarily for the truncation of the virtual orbital space, and since it is used consistently throughout this study, we will henceforth simply refer to the method as CCSD(T).

2.2. Reduction Potential and pK_a Calculation Details. To perform the reduction potential, $E°$, and the pK_a calculations, we employed the standard protocol in which electronic structure calculations are used in combination with an experimental reference.[59]

For the calculations of the reduction potential associated with a given redox pair, we use

$$E°(\mathrm{Co}^{\mathrm{II/I}}) = -\frac{\Delta G°_{\mathrm{r}}}{F} + E°(\mathrm{Co}^{\mathrm{II/I}})(\mathrm{ref}) \quad (1)$$

where F is the Faraday constant and $E°(\mathrm{Co}^{\mathrm{II/I}})(\mathrm{ref}) = -0.72$ (V vs SCE) is the experimental reference value for complex **1** in acetonitrile.[21,34] Here, $\Delta G°_{\mathrm{r}}$ is the free energy difference between the redox couple of interest and that of the reference system

DOI: 10.1021/acscatal.6b01387
ACS Catal. 2016, 6, 6114−6123

$$\Delta G^{\circ}_{r} = G^{\circ}_{Co^{I}} + G^{\circ}_{Co^{II}}(\mathrm{ref}) - G^{\circ}_{Co^{II}} - G^{\circ}_{Co^{I}}(\mathrm{ref}) \quad (2)$$

where $G^{\circ}_{Co^{I}}(\mathrm{ref})$ and $G^{\circ}_{Co^{II}}(\mathrm{ref})$ are computed using complex **1**. Each free energy term on the right-hand side of eq 2 is calculated using

$$G^{\circ}_{\xi} = \varepsilon_0^{(\xi)}(\mathrm{CCSD(T)\text{-}in\text{-}DFT}) + G_{\mathrm{corr}}^{(\xi)}(\mathrm{DFT}) + G_{\mathrm{solve}}^{(\xi)}(\mathrm{DFT}) \quad (3)$$

where $\xi = Co^{I}$, Co^{II} indicates the redox state of the system. Here, ε_0 is the total electronic energy, G_{corr} is the gas-phase correction to Gibbs free energy based on harmonic vibrational frequencies, and G_{solve} is the solvation correction to the Gibbs free energy based on the conductor-like polarizable continuum model (C-PCM);[60] for each quantity, the level of electronic structure theory used for the computation is indicated in parentheses. Following previous work on cobalt-based hydrogen evolution catalysts,[61,62] the C-PCM calculations are employed using Bondi radii[63] and including nonelectrostatic contributions from dispersion,[64] repulsion,[65] and cavity formation.[66]

For the pK_a calculations reported in this study, we use

$$\mathrm{p}K_a = \frac{\Delta G^{\circ}_{r}}{\ln(10)RT} + \mathrm{p}K_a(\mathrm{ref}) \quad (4)$$

where R is the molar gas constant and pK_a(ref) = 13.3 is the experimental reference value for $Co^{III}H(dmgBF_2)$ in acetonitrile.[67] ΔG°_{r} is the free energy difference between the proton-transfer processes of the system of interest and that of the reference system, in analogy with eq 2.

2.3. Geometry Optimizations and Reaction Barriers. All reactant and product geometries in this study are optimized at the at the B3P86/6-311+G(d,p) level of theory using Gaussian 09.[68] All of the DFT results reported in this paper are obtained at this level of theory. All Co complexes are described in their low-spin state, as is suggested by experiment[9,69] and supported by B3P86/6-311+G(d,p) calculations which indicate that the high-spin configuration for optimized geometries of both complex **1** and complex **2** with methyl substitution is at least 20 kcal/mol higher than the corresponding low-spin configuration in the Co^{I}, Co^{II}, and Co^{III}(H) states.

For all numerical results reported in this work, including those associated with both complexes **1** and **2**, the solvent molecule CH_3CN occupies the axial ligand positions. Only for comparison of the computationally optimized geometry of complex **2** with the experimental crystal structure do we consider a system with bromide axial ligands.

For both complexes **1** and **2**, the optimized geometries exhibit two CH_3CN axial ligands in the Co^{II} redox state, one CH_3CN axial ligand in the Co^{I} state, and one CH_3CN axial ligand in the Co^{III} H state. Upon reduction from Co^{II} to Co^{I}, it is found that, in both complexes **1** and **2**, one of the axial ligands detaches during the geometry optimization; note that the energy contributions from this detached ligand exactly cancel in our reduction potential calculations (eq 2). The reduction potential calculations are performed with the pendant pyridyl group in the equatorial configuration for both the Co^{II} and Co^{I} states, which is computed to be the more stable configuration and which is straightforwardly compared to the experimental reduction potentials at 0 equiv of external acid. In contrast to the previously reported structure for the H-substituted version of complex **2** (R = −H),[17,37] we find that the methyl-substituted pyridyl group introduces geometric frustration that favors the equatorial configuration. All optimized geometries are reported in the Supporting Information.

For the intramolecular proton transfer reaction of complex **2**, we consider the pendant pyridyl group to be in the endo configuration for both the Co^{I} reactant and the Co^{III}(H) product, as illustrated in Figure 3. The geometries along the minimum-energy pathway between the reactant and product are computed at the B3P86/6-311+G(d,p) level of theory, using the synchronous transit-guided quasi-Newton method[70] to locate the energy barrier, which is confirmed to have only a single imaginary vibrational frequency, and then the intrinsic reaction coordinate is constructed with a Hessian-based predictor-corrector integrator.[71] Using these geometries along the DFT-computed minimum-energy pathway for the proton-transfer reaction, we then compute single-point calculations at the CCSD(T)-in-DFT level of theory; this was found to be necessary because CCSD(T) and DFT differ in both the energy and position of the reaction barrier. For the proton-transfer reaction associated with each ligand-substituted version of complex **2**, we thus perform at least 25 CCSD(T)-in-DFT single-point calculations; the total number of CCSD(T)-in-DFT calculations reported in this study exceeds 200.

For the intramolecular proton transfer reaction of complex **1**, we use the climbing image nudged elastic band method (CI-NEB),[72] as implemented in the CP2K package,[73] to explore the transition path in order to capture multiple transition states for a long reaction path. The reactant Co^{I}(OH) and the product Co^{III}(H) geometries are preoptimized and kept fixed during the NEB calculations. The initial path is linearly interpolated between the geometries of the reactant and product with 30 images. DFT energies and gradient were calculated with the Gaussian and plane-wave (GPW) mixed basis method,[74] with the molecule in a cubic box of side length 25 Å. Core electrons are modeled using Goedecker−Teter−Hutter (GTH) type norm-conserving pseudopotentials,[75] and the valence orbitals are expanded in the DZVP basis set for Co and TZV2P basis set for all other atoms,[23,51] together with a plane-wave auxiliary basis with a 300 Ry energy cutoff. Plane-wave electrostatic contributions were computed using the Poisson solver of Martyna and Tuckerman.[76] Results for the CI-NEB calculations are reported using the Becke−Perdew (BP86) exchange-correlation functional[49,50] and agree closely with those obtained using the Perdew−Burker−Ernzerhof (PBE) functional with the Grimme DFT-D3[77] dispersion correction.

2.4. Electrochemical Measurements. Electrochemical measurements were recorded with a CH Instruments 630-C electrochemistry analyzer using the CHI software package (version 8.09). Cyclic voltammetry data (100 mV/s scan rate) were acquired for solutions of 0.5 mM $[Co(CH_2MepyrH\text{-}dopnH)Br_2]Br$ (i.e., complex **2** with methyl substitution) in MeCN containing varying amounts of $[PhNH_3][OTf]$ (0−8 equiv). Solutions contained 0.1 M $[n\text{-}Bu_4N][ClO_4]$ as supporting electrolyte and were purged with N_2 prior to data collection. For each measurement, a 0.195 cm^2 glassy-carbon disk was used as the working electrode (Pine Instrument Co.), a Pt wire was used as the auxiliary electrode, and a Ag wire was used as the reference electrode. Potentials were internally referenced against the reversible Fc/Fc^{+} couple (+0.38 V vs SCE in MeCN). See the Supporting Information for preparation and characterization data of complex **2**.

DOI: 10.1021/acscatal.6b01387
ACS Catal. 2016, 6, 6114−6123

3. RESULTS AND DISCUSSION

3.1. Proton-Shuttling Pathways in Complex 2 versus Complex 1. The current section compares the energy barriers associated with the intramolecular proton-transfer reaction (step B in Figure 2) in complexes **1** and **2**.

We begin by comparing the energy profiles for the intramolecular proton-transfer reaction in complex **2** with methyl substitution obtained using CCSD(T), DFT, and CCSD(T)-in-DFT. Figure 4A presents the energies from each method along the geometries of the intrinsic reaction coordinate.

Consideration of the black and blue curves in Figure 4A reveals that DFT, at least with the B3P86 exchange-correlation functional, introduces significant errors in the description of the energy profile in comparison to CCSD(T). Interestingly, these errors manifest in three different ways: the magnitude of the barrier to the reaction, the position of the barrier along the minimum energy pathway, and the relative energy of the reactant and product species. Although we recognize that the use of other exchange-correlation functionals may affect the details of this figure, this highlights the well-known limitations of DFT in systems involving transition-metal complexes.

Figure 4 also demonstrates that the CCSD(T)-in-DFT embedding calculations accurately recover the results of CCSD(T) performed over the full system. In Figure 4B, the subset of atoms that are described at the CCSD(T) level are indicated in solid colors, whereas the remainder of the system is described using DFT; Figure 4C presents the corresponding partitioning of the electronic density. Note that only the transition-metal center, the transferring proton, and the nearest covalently attached atoms are described at the CCSD(T) level of theory. Using this subsystem partitioning, the red curve in Figure 4A presents the CCSD(T)-in-DFT energy profile along the proton-transfer intrinsic reaction coordinate. It is clear that the embedding calculations essentially eliminate the errors of DFT in comparison to CCSD(T). This good agreement is particularly encouraging, given that the CCSD(T)-in-DFT method leads to an approximately 15 times reduction of the computational cost of the energy calculations for this system in comparison to CCSD(T) performed over the full system. The accuracy of CCSD(T)-in-DFT embedding, in combination with its reduction in computational cost, illustrates the usefulness of the method in applications involving reactions at transition-metal centers; we employ the embedding method throughout the remainder of this study unless otherwise stated.

Figure 5 presents the energy profile for the intramolecular proton-transfer reaction in complex **1** obtained using CCSD(T)-in-DFT. In contrast with relatively low free energy barrier of 8 kcal/mol found for complex **2** (Figure 4), complex **1** exhibits a far larger proton-transfer barrier of approximately 60 kcal/mol. Surmountable reaction barriers in electrocatalytic systems are typically lower than 20 kcal/mol.[6,36,78] The main contributing factor to this large barrier in complex **1** is the large proton transfer distance from the second oxime protonation site to the cobalt center; note that the first oxime protonation site, which bridges the two oxygens (Figure 3), remains protonated throughout the transfer process. Whereas the proton-transfer distance from the pendant pyridyl group to cobalt in complex **2** is only ∼0.7 Å, the intramolecular proton-transfer reaction in complex **1** needs to span 3.4 Å to reach the cobalt center. These results suggest that whereas complex **2** provides a kinetically viable intramolecular proton-shuttling pathway, complex **1** does not.[21] The role of bimolecular proton (or H atom) transfer pathways are not explicitly considered herein.

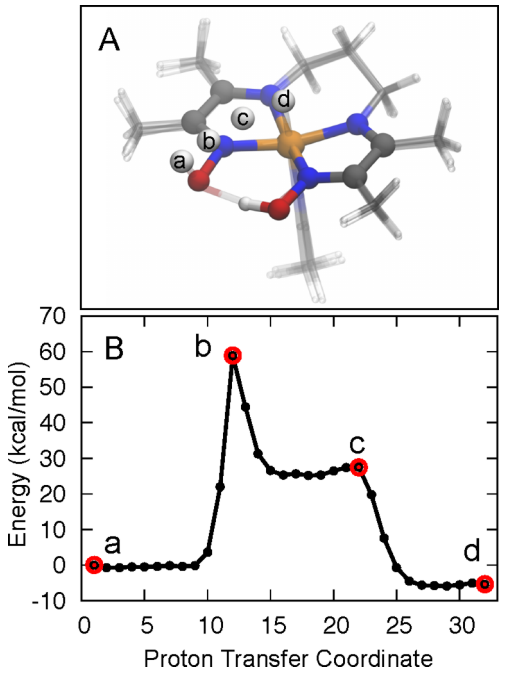

Figure 5. (A) Partitioning of complex **1** into atoms that are treated using CCSD(T) (solid ball−stick) and DFT (transparent stick) in the CCSD(T)-in-DFT calculations. Various positions of the transferring proton along its reaction profile are highlighted with larger radius and labeled with indexes a−d. (B) Energy profiles for the intramolecular proton-transfer reaction in complex **1**, obtained using CCSD(T)-in-DFT. The points along the reaction profile depicted in part A are indicated in red.

3.2. Proton Binding Sites and Their Influence on $Co^{II/I}$ Reduction Potential. Figure 6A presents experimental cyclic voltammetry (CV) measurements for complex **2**, as well as a comparison between the crystal structure and computationally optimized geometry for this compound. Throughout this section, all results for complex **2**, both computational and experimental, correspond to the system with methyl substitution. The CV measurements for complex **2** (Figure 6A) reveal a reversible $Co^{II/I}$ redox couple at −0.72 mV vs SCE, accompanied by a prewave feature that is assigned to a small degree of proton reduction from the pendant pyridinium substituent. Upon addition of increasing concentrations of anilinium, there is a positive shift in the peak potential to −0.60 mV (indicated by arrows). A similar shift is observed for complex **1**, as has been previously reported[21,34,35] and confirmed in the current work (see the Supporting Information).

The shift of the reduction potential upon increasing acid concentration for both complexes **1** and **2** indicates that the available proton-binding sites influence the reduction potential. Previous experiments have found that, in the absence of protonation sites on the ligands, qualitatively different behavior is observed in the CV curves upon addition of acid; the shifts observed in Figure 6A are thus attributed to the sensitivity of the reduction potential to ligand protonation.[21,34,35,62,79] For complex **1**, the oxime group is the only apparent ligand protonation site, whereas complex **2** can undergo protonation at either the oxime or pyridyl groups. With 0 equiv of added

DOI: 10.1021/acscatal.6b01387
ACS Catal. 2016, 6, 6114−6123

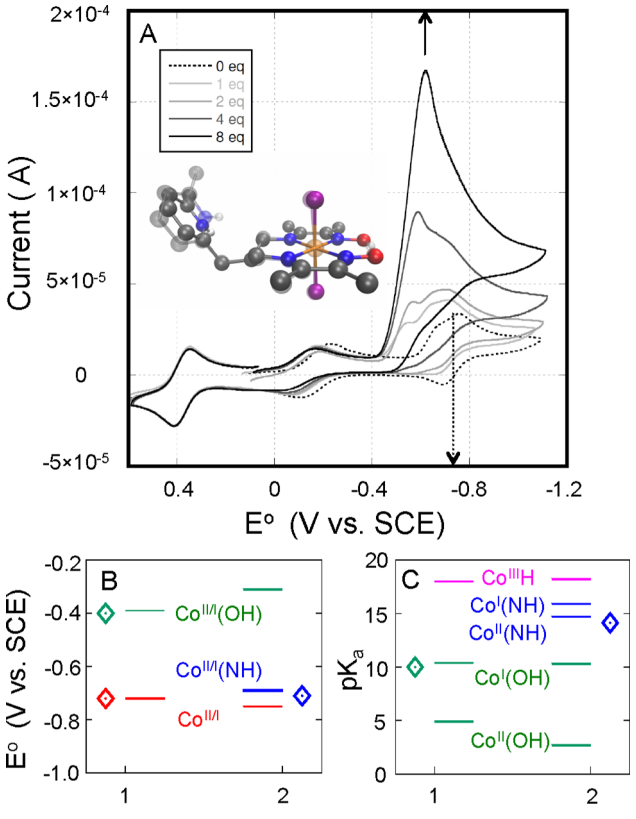

Figure 6. (A) Cyclic voltammetry measurements for a 0.5 mM solution of complex **2** (R = $-CH_3$) in acetonitrile, with increasing concentrations of $[PhNH_3][OTf]$ acid (0.1 M $[n\text{-}Bu_4N][ClO_4]$ supporting electrolyte; 100 mV/s scan rate; N_2 atmosphere; glassy-carbon working electrode; solutions contain $Fe(C_5H_5)_2$ as an internal standard referenced to +0.38 V vs SCE) Inset: crystal structure for complex **2** (solid), superimposed with the calculated optimized geometry in the equatorial configuration (transparent). (B) Comparison of experimental and calculated reduction potentials for complexes **1** and **2** in various states of protonation, with experimental results indicated using diamonds and with the calculated CCSD(T)-in-DFT results indicated using lines. (C) Comparison of experimental and calculated pK_a values for complexes **1** and **2** in various redox states, with experimental results indicated using diamonds and with the calculated CCSD(T)-in-DFT results indicated using lines.

acid, the CV curve for complex **2** closely resembles that of **1** (Figure S4 in the Supporting Information), despite the fact that the pyridyl group in complex **2** is expected to be protonated from the crystal structure. Upon addition of acid, the CV curves for both complexes **1** and **2** shift to more positive reduction potentials, and the similarity of these shifts in the two complexes suggests that they are due to the oxime group, which is a shared feature; the shift of the reduction potential in the CV curve for complex **2** is not attributed to protonation of the pyridyl group, which is assumed to remain protonated throughout the range of conditions studied here.

With use of these observations, Figure 6B summarizes both the experimental and computed values for the reduction potentials of complexes **1** and **2**. In this figure panel, and throughout the discussion of the results, we employ a labeling scheme in which "Co" indicates the molecular composition of either complex **1** or **2**, as depicted in Figure 3, while "Co(XH)" indicates that molecular composition with additional protonation at site X, where X = O, N indicates the oxime and pyridine groups, respectively. The experimental value for the reduction potential associated with the $Co^{II/I}(NH)$ redox pair of complex **2** was taken from the CV curve of complex **2** at 0 equiv of acid, indicated with the blue diamond in Figure 6B. The experimental value for the reduction potential associated with the $Co^{II/I}$ redox pair of complex **1** was taken from the CV curve of complex **1** at 0 equiv of acid,[21,34] indicated with the red diamond. The experimental value for the reduction potential associated with the $Co^{II/I}(OH)$ redox pair of complex **1** was taken from the CV curve of complex **1** at 3 equiv of strong acid,[21,34] indicated with the green diamond. No experimental reduction potential for the $Co^{II/I}(OH)$ redox pair of complex **2** is reported, since the relative pK_as of the second oxime protonation site and the pyridine site (see Figure 6C) are such that the dominant species is never that for which the second oxime site is protonated while the pyridine is not.

Figure 6B also presents the calculated reduction potentials for the two complexes, obtained using CCSD(T)-in-DFT. Calculated reduction potentials are reported for the $Co^{II/I}$ redox pairs associated with both complexes **1** and **2** in their various states of ligand protonation. We note that, for all three available comparisons between the experimentally and computationally obtained reduction potentials in Figure 6B, good agreement is observed.

Figure 6C presents both calculated and experimental pK_a values for the pyridyl (N) and second oxime (O) proton-binding sites. For complex **1** in the Co(I) redox state, the experimental pK_a for the second oxime site can be interpreted from previous experimental results (see the Supporting Information for details) to be 10.0 (green diamond).[21] The experimental pK_a for the pyridyl group has not been directly measured for complex **2**; however, since this site is relatively uncoupled from the redox state of the cobalt center, we can obtain an experimental pK_a value of 14.3 from 2,6-dimethylpyridine (blue diamond).[80] Computed values for each of the pK_a values of the two complexes in their various redox states are also reported from CCSD(T)-in-DFT calculations (solid lines), demonstrating good agreement with the available experimental results.

Several additional observations regarding Figure 6C are worthwhile. First, we note that the experimentally used acid in the CV measurements ($[PhNH_3][OTf]$) has a pK_a of 10.7;[21] the results in Figure 6C are thus consistent with our analysis of Figure 6A, in which it was assumed that the second oxime site changes protonation states as a function of increasing acid concentration while the pyridyl group remains protonated at all acid concentrations. Second, note that the pK_a for the $Co^{I}(OH)$ species of complex **1** is determined from both experiment and computation to be approximately 10, while the unreduced $Co^{II}(OH)$ species of complex **1** is calculated to have a substantially lower pK_a of approximately 5. This large computed shift in the calculated pK_a of the second oxime site is sensible, given that the cobalt center and oxime sites are strongly coupled, and the result is consistent with the sizable difference of the reduction potential for complex **1** upon deprotonation of the second oxime site (Figure 6B).

Finally, we note from Figure 6C that the pK_a for the pyridyl group in complex **2** is largely independent of the redox state of the cobalt center. This result is particularly encouraging, given that it was previously found (Figure 4) that complex **2** provides a kinetically viable pathway for performing the intramolecular proton shuttling step in the hydrogen reduction pathway (i.e., step B in Figure 2). Given that complex **2** facilitates the intramolecular proton shuttling step, and given that complex **2**

DOI: 10.1021/acscatal.6b01387
ACS Catal. 2016, 6, 6114−6123

decouples the energetics of deprotonating the pyridyl group from the redox state of the cobalt center, it follows that this complex is a promising candidate for achieving hydrogen evolution catalysis while avoiding the deleterious coupling between the energetics of metal site reduction and the kinetics of metal hydride formation. With this motivation, the next section explicitly examines the degree to which complex **2** successfully decorrelates $Co^{II/I}$ reduction (step A in Figure 2) and hydride formation (step B in Figure 2) in the hydrogen reduction pathway.

3.3. Additional Analysis of Protonation. Although the WF-in-DFT method overcomes substantial errors with respect to DFT in the proton-transfer reaction energy profiles (see Figure 4A and Figures S8 and S9 in the Supporting Information), it is found that both WF-in-DFT and DFT at least give qualitatively similar results for the calculation of reduction potentials and pK_a values for the systems studied here (see Figure 6 and Figure S10 in the Supporting Information). We thus employ the DFT (B3P86/6-311+G-(d,p)) level of theory for the calculated pK_a values employed in this section for additional mechanistic analysis.

Table 1 reports pK_a values for both equatorial and axial pyridyl group in complex **2** in the Co^{II} redox state

Table 1. Calculated pK_a Values for the Pyridyl and Oxime Groups in Complex 2 with Methyl Substitution, Considering both the Axial and Equatorial Configurations of the Pendant Pyridyl Group[a]

complex **2**	axial	equatorial
pK_a[Co^{II}(N**H**)]	14.3	14.7
pK_a[Co^{I}(NH)(O**H**)]	8.8	8.4
pK_a[Co^{I}(O**H**)]	10.3	10.3
pK_a[Co^{III}H(N**H**)]	15.6	15.0

[a]Values correspond to deprotonation of the hydrogen indicated in bold.

(pK_a[Co^{II}(N**H**)]). Note the relative similarity of the pyridyl pK_a in these two configurations. This result suggests that the driving force for protonation of the pyridyl group is relatively insensitive to the configuration of that pyridyl group, which is in contrast to the proton shuttle in previously studied cobalt tetraphosphine complexes.[33]

In addition, Table 1 reports pK_a values for the second oxime group in complex **2** with the Co^{I} redox state and a preprotonated pyridyl group (pK_a[Co^{I}(NH)(O**H**)]). These pK_a values are lower by almost 1.5 units in comparison to those for the complex without the preprotonation of the pyridyl group (pK_a[Co^{I}(O**H**)]). It is thus expected to be difficult to protonate the second oxime following preprotonation of the pyridyl group at the low concentration of weak acid used in the current study. This is also supported by the finding that the experimental CV peaks are not fully shifted to the theoretical value of −0.4 V in Figure 6A. Taken together, these results justify our consideration of a singly protonated complex in the computed PT reaction profiles for the Co^{I} complex (Figure 4).

Finally, we note from Table 1 that the pK_a for the pyridyl group following intramolecular proton transfer (pK_a[Co^{III}H-(N**H**)]) is higher than that of the pyridyl group for the species that is expected to be protonated in advance of the intramolecular transfer (pK_a[Co^{II}(N**H**)]), suggesting that reprotonation of the pyridyl group after intramolecular proton transfer is rapid.

3.4. Decoupling Co Reduction from the Kinetics of Co-Hydride Formation. We now investigate the degree to which complex **2** successfully avoids the deleterious anti-correlation between the energetics of $Co^{II/I}$ reduction (step A in Figure 2) from the kinetics of Co^{III} hydride formation (step B in Figure 2).

Figure 7 presents the theoretically predicted $Co^{II/I}$ reduction potential (blue squares) and the intramolecular proton-transfer

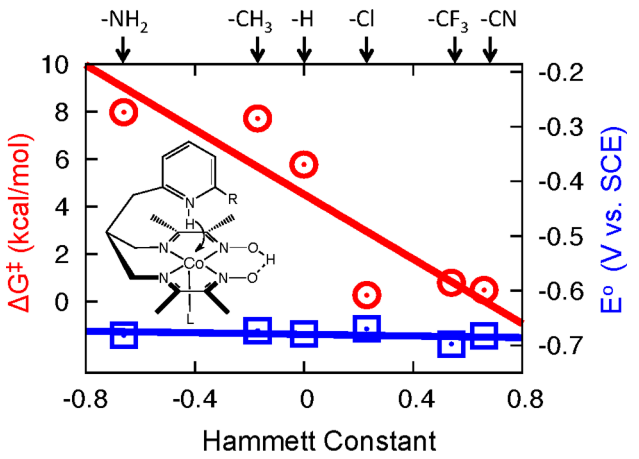

Figure 7. Free-energy barrier ($\Delta G^{\ddagger}$, red circles) for the intramolecular proton-transfer reaction associated with Co^{III}(H) formation in complex **2**, plotted as a function of the Hammett constant of the benzoic acid para substituent, and the $Co^{II/I}$ reduction potential (blue squares) for the corresponding systems. All calculations are performed using CCSD(T)-in-DFT embedding, and the lines indicate linear fits of the data. The reduction potential (y axis at right) is plotted on the same energy scale as the reaction barrier (x axis at left).

reaction barrier (red circles) for complex **2** with a range of pyridyl substituents (−R). The results are plotted as a function of Hammett constant,[81] which quantifies the electron-withdrawing propensity of each substituent. All reaction barriers and reduction potentials are computed using CCSD(T)-in-DFT embedding.

It is immediately clear from the figure that, whereas the proton-transfer barriers exhibit a strong, linear dependence on the Hammett constant, the reduction potential is nearly independent of the pyridyl substituent group. Complex **2** avoids the unwanted anti-correlation between these two steps, because the pyridyl substituent is strongly coupled to the proton-transfer donor while being negligibly coupled to the transition-metal center that accepts the transferring electron. The results in Figure 7 suggest that, by employing strongly electron-withdrawing pyridyl substituents in complex **2**, the intrinsic proton-transfer barrier for hydride formation can be nearly eliminated, without affecting the energetics of the $Co^{II/I}$ reduction potential. Complex **2** is thereby predicted to avoid the unwanted anti-correlation between these two steps that have been encountered in other Co-based hydrogen reduction catalysts,[8,28−31] for which substituent group modifications are coupled to both the proton-transfer and electron-transfer acceptors.[8,27] Note that if the intrinsic proton-transfer barrier for hydride formation is sufficiently reduced, step B in Figure 2 will no longer be kinetically limiting, and further improvement of the catalyst will necessarily focus on other steps in the catalytic pathway. Regardless, complex **2** illustrates a possible design principle to enable higher turnover frequencies for hydrogen evolution without compromising the reduction

DOI: 10.1021/acscatal.6b01387
ACS Catal. 2016, 6, 6114−6123

potential, and more generally, the use of substituent groups to separately couple to proton-transfer donors and electron-transfer acceptors (or vice versa) enables the possibility of control over the flow of positive and negative charges in catalytic pathways. Before proceeding, we emphasize several aspects of the results in Figure 7.

First, the barrier heights for the intramolecular proton-transfer reported in Figure 7 correspond to a reaction pathway for which the pendant pyridyl group in complex **2** occupies the axial configuration throughout the transfer event, as illustrated in the inset of the figure. This deserves mention, because the equatorial configuration for the $Co^{I}(NH)$ species is calculated using DFT to have a free energy that is 2.7 kcal/mol more stable than that of the axial configuration, suggesting that the axial conformation will be significantly less populated in the thermal ensemble. However, the available experimental data suggest that this preference for equatorial configuration of the pendant pyridyl group may hinder its role as an intramolecular proton shuttle. Specifically, comparison of the electrochemical data for complexes **1** and **2** over a range of acid concentrations, either in terms of the rotating-disk volammograms (Figure S5 in the Supporting Information) or in terms of the cyclic voltammograms (Figure 6 and Figure S4 in the Supporting Information), suggests that the two complexes operate via a similar catalytic mechanism, with little enhancement in catalytic activity in complex **2** due to the pendant pyridyl group. These results highlight a critical need for effective conformational control in the catalyst structure in future designs that would thereby maximize the effective concentration of the shuttling functionality near the metal site.

Second, we note that the analysis presented here, which is based on the catalytic pathway shown in Figure 2, assumes that protonation of the cobalt center to form the Co^{III} hydride proceeds via intramolecular transfer from the pyridyl site, rather than via direct protonation from the solvent environment or via alternative bimolecular pathways. Given the high energy of the Co^{IV} hydride species calculated using DFT calculations,[82] it is reasonable to assume that any proton transfer to the cobalt center will be preceded by the $Co^{II/I}$ reduction step. Furthermore, given the relatively high pK_a for the pyridyl group in complex **2** (as seen in Figure 6C), it is expected that the pyridyl group is protonated prior to the $Co^{II/I}$ reduction step. Therefore, when the $Co^{II/I}$ reduction step occurs, the pyridyl group will be protonated, such that it is "primed" to perform the intramolecular proton-transfer step, which might be expected (on the basis of the relatively low intramolecular proton-transfer barriers seen in Figure 7) to kinetically outcompete the bimolecular proton transfer from the surrounding solvent environment. This assumption regarding the possible predominance of the intramolecular proton-shuttling mechanism, in favor of direct proton transfer to the cobalt center from the solvent, is acknowledgedly qualitative and expected to be most plausible under conditions of low acid concentration. After step B in Figure 2, it is assumed that the pyridyl group is reprotonated by the external acid; the torsional flexibility and accessibility of this pyridyl group, along with its high pK_a, suggests that this reprotonation will readily occur.

Third, while the current study assumes that the kinetic bottleneck for the catalytic pathway in Figure 2 is the proton-transfer reaction in step B, other work has found that for other Co- and Ni-based hydrogen reduction catalysts the kinetic bottleneck may be associated with the hydrogen evolution in step C.[9,23,24,32,83] In particular, for complex **1**, an extensive recent computational study[36] concluded that the rate-limiting step in the catalytic cycle is formation of hydrogen via coupling of the Co^{II} hydride with a proton on a neighboring oxime site. In Figure S11 in the Supporting Information, we explicitly examine the hydrogen evolution step for complex **2** and find that, unlike complex **1**, it offers a low-energy pathway for hydrogen formation via coupling of the Co^{II} hydride with a proton on the pendant pyridyl group. This analysis thus supports our focus on the proton transfer reaction in step B as the kinetic bottleneck for complex **2**.

Finally, we note that complex **2** is interesting to compare with other systems that have been designed to introduce a proton-shuttling mechanism into the catalytic pathway for hydrogen evolution. Previous work includes both the "hangman" porphyrin group by Nocera and co-workers[22,84,85] that appears to act as an intramolecular proton shuttle to the meso carbon of the porphyrin ring[86,87] and a flexible pendant amine group by DuBois and co-workers[32] that acts as an intramolecular proton shuttle to the transition-metal center.[88] In particular, the Ni/Co-based pendant amine systems[23,32,33] appear to require significant conformation rearrangements within each catalytic cycle,[33] thus exhibiting an issue which is similar to that discussed above for the axial/equatorial conformational flexibility of the pyridyl pendant group in complex **2**. If it is possible in future work to lock the pyridyl pendant group in complex **2** into the axial configuration, as suggested here, this may lead to the development of hydrogen reduction catalysts with advantages that include (i) rapid intramolecular proton shuttling, (ii) no required conformational changes within or between catalytic cycles, and (iii) avoidance of the deleterious coupling between the energetics of Co reduction and the kinetics of intramolecular Co hydride formation.

4. CONCLUSIONS

In this work, a recently developed wavefunction-in-DFT embedding method is combined with the synthesis and electrochemical analysis of a new cobalt pyridine-diimine-dioxime complex in the context of hydrogen evolution catalysis. The WF-in-DFT method is shown to overcome significant deficiencies of conventional DFT in describing the reaction energies and kinetic barriers associated with steps in the catalytic pathway, thus providing the accuracy of high-level wave function methods (in this case, CCSD(T)) at a greatly reduced computational cost. Comparison of experimental electrochemical analysis and WF-in-DFT calculations provides benchmarking of the computational results and yields insight into the state of ligand protonation for hydrogen evolution reaction intermediates. Furthermore, WF-in-DFT calculations of the hydrogen evolution pathway suggest that complex **2**, which introduces a pendant pyridyl moiety to serve as an intramolecular proton shuttle for the formation of the metal hydride intermediate, may successfully remove the deleterious coupling between the energetics of metal site reduction and the kinetics of metal hydride formation, which has been a significant obstacle in the design of efficient hydrogen evolution catalysts. Alternative H_2 evolution scenarios whereby generation of an isomer of an on-path Co−H intermediate are not considered in this study but should still be kept in mind.[89,90]

The work presented here demonstrates a powerful new theoretical methodology for the accurate description of transition-metal catalysts, as well as evidence in support of a synthetic design principle for decoupling the flow of electrons

DOI: 10.1021/acscatal.6b01387
ACS Catal. 2016, 6, 6114−6123

and protons in catalytic pathways, potentially enabling the development of of hydrogen evolution catalysts that operate at high turnover rate and low overpotential. Experimentally demonstrating enhanced catalysis rates at lower overpotential via the theoretically guided decoupling of energy costs and kinetic barriers is the subject of ongoing studies.

■ ASSOCIATED CONTENT

Supporting Information

The Supporting Information is available free of charge on the ACS Publications website at DOI: 10.1021/acscatal.6b01387.

Experimental procedures and data, including the synthesis and crystal structure of complex **2** and additional electrochemistry data for complexes **1** and **2**, and molecular geometries from the computations (PDF)

■ AUTHOR INFORMATION

Corresponding Authors

*E-mail for J.C.P.: jpeters@caltech.edu.
*E-mail for T.F.M.: tfm@caltech.edu.

Present Addresses

[‡]Department of Chemistry, University of Rochester, 120 Trustee Road, Rochester, New York 14627, United States
[§]Department of Chemistry, Purdue University, 560 Oval Drive, West Lafayette, Indiana 47907, United States
[∥]Department of Chemistry, University of Minnesota, 207 Pleasant Street SE, Minneapolis, Minnesota 55455, United States

Notes

The authors declare no competing financial interest.

■ ACKNOWLEDGMENTS

This work was supported by the Air Force Office of Scientific Research (USAFOSR) under Grant No. FA9550-11-1-0288, the (U.S.) Department of Energy (DOE) under Grant No. DE-SC0006598, and by the NSF Center for Chemical Innovation Solar Fuels Grant CHE-1305124. P.H. thanks Kara Bren and Richard Eisenberg for helpful discussions. Computing resources were provided by the National Energy Research Scientific Computing Center (NERSC) (DE-AC02-05CH11231) and XSEDE (TG-CHE130108).

■ REFERENCES

(1) (a) Lewis, N. S.; Nocera, D. G. *Proc. Natl. Acad. Sci. U. S. A.* **2006**, *103*, 15729−15735. (b) Gray, H. B. *Nat. Chem.* **2009**, *1*, 7−7.
(2) Artero, V.; Chavarot-Kerlidou, M.; Fontecave, M. *Angew. Chem., Int. Ed.* **2011**, *50*, 7238−7266.
(3) Kaeffer, N.; Chavarot-Kerlidou, M.; Artero, V. *Acc. Chem. Res.* **2015**, *48*, 1286−1295.
(4) Raugei, S.; Helm, M. L.; Hammes-Schiffer, S.; Appel, A. M.; O'Hagan, M.; Wiedner, E. S.; Bullock, R. M. *Inorg. Chem.* **2016**, *55*, 445−460.
(5) McKone, J. R.; Marinescu, S. C.; Brunschwig, B. S.; Winkler, J. R.; Gray, H. B. *Chem. Sci.* **2014**, *5*, 865−878.
(6) Solis, B. H.; Hammes-Schiffer, S. *Inorg. Chem.* **2014**, *53*, 6427−6443.
(7) Bullock, R. M.; Appel, A. M.; Helm, M. L. *Chem. Commun.* **2014**, *50*, 3125−3143.
(8) Hu, X.; Brunschwig, B. S.; Peters, J. C. *J. Am. Chem. Soc.* **2007**, *129*, 8988−8998.
(9) (a) Dempsey, J. L.; Winkler, J. R.; Gray, H. B. *J. Am. Chem. Soc.* **2010**, *132*, 16774−16776. (b) Dempsey, J. L.; Winkler, J. R.; Gray, H. B. *J. Am. Chem. Soc.* **2010**, *132*, 1060−1065.
(10) (a) Lazarides, T.; McCormick, T.; Du, P.; Luo, G.; Lindley, B.; Eisenberg, R. *J. Am. Chem. Soc.* **2009**, *131*, 9192−9194. (b) Du, P.; Knowles, K.; Eisenberg, R. *J. Am. Chem. Soc.* **2008**, *130*, 12576−12577.
(11) (a) McNamara, W. R.; Han, Z.; Yin, C.-J. M.; Brennessel, W. W.; Holland, P. L.; Eisenberg, R. *Proc. Natl. Acad. Sci. U. S. A.* **2012**, *109*, 15594−15599. (b) McNamara, W. R.; Han, Z.; Alperin, P. J.; Brennessel, W. W.; Holland, P. L.; Eisenberg, R. *J. Am. Chem. Soc.* **2011**, *133*, 15368−15371.
(12) (a) Kleingardner, J. G.; Kandemir, B.; Bren, K. L. *J. Am. Chem. Soc.* **2014**, *136*, 4−7. (b) Bacchi, M.; Berggren, G.; Niklas, J.; Veinberg, E.; Mara, M. W.; Shelby, M. L.; Poluektov, O. G.; Chen, L. X.; Tiede, D. M.; Cavazza, C.; Field, M. J.; Fontecave, M.; Artero, V. *Inorg. Chem.* **2014**, *53*, 8071−8082.
(13) Levy, N.; Mahammed, A.; Kosa, M.; Major, D. T.; Gross, Z.; Elbaz, L. *Angew. Chem., Int. Ed.* **2015**, *54*, 14080−14084.
(14) Muresan, N. M.; Willkomm, J.; Mersch, D.; Vaynzof, Y.; Reisner, E. *Angew. Chem., Int. Ed.* **2012**, *51*, 12749−12753.
(15) Andreiadis, E.; Jacques, J.; Tran, P. T.; Leyris, A.; Chavarot-Kerlidou, M.; Jousselme, B.; Matheron, M.; Pécaut, J.; Palacin, S.; Fontecave, M.; Artero, V. *Nat. Chem.* **2012**, *5*, 48−53.
(16) Kaeffer, N.; Morozan, A.; Artero, V. *J. Phys. Chem. B* **2015**, *119*, 13707−13713.
(17) Probst, B.; Guttentag, M.; Rodenberg, A.; Hamm, P.; Alberto, R. *Inorg. Chem.* **2011**, *50*, 3404−3412. PMID: 21366324.
(18) Oberholzer, M.; Probst, B.; Bernasconi, D.; Spingler, B.; Alberto, R. *Eur. J. Inorg. Chem.* **2014**, *2014*, 3002−3009.
(19) Guttentag, M.; Rodenberg, A.; Kopelent, R.; Probst, B.; Buchwalder, C.; Brandstätter, M.; Hamm, P.; Alberto, R. *Eur. J. Inorg. Chem.* **2012**, *2012*, 59−64.
(20) Zhang, P.; Jacques, P.-A.; Chavarot-Kerlidou, M.; Wang, M.; Sun, L.; Fontecave, M.; Artero, V. *Inorg. Chem.* **2012**, *51*, 2115−2120. PMID: 22313315.
(21) Jacques, P.-A.; Artero, V.; Pécaut, J.; Fontecave, M. *Proc. Natl. Acad. Sci. U. S. A.* **2009**, *106*, 20627−20632.
(22) Roubelakis, M. M.; Bediako, D. K.; Dogutan, D. K.; Nocera, D. G. *Energy Environ. Sci.* **2012**, *5*, 7737−7740.
(23) O' Hagan, M.; Shaw, W. J.; Raugei, S.; Chen, S.; Yang, J. Y.; Kilgore, U. J.; DuBois, D. L.; Bullock, R. M. *J. Am. Chem. Soc.* **2011**, *133*, 14301−14312.
(24) Mandal, S.; Shikano, S.; Yamada, Y.; Lee, Y.-M.; Nam, W.; Llobet, A.; Fukuzumi, S. *J. Am. Chem. Soc.* **2013**, *135*, 15294−15297.
(25) Muckerman, J. T.; Fujita, E. *Chem. Commun.* **2011**, *47*, 12456−12458.
(26) Structural isomers of the Co^{III} hydride intermediate where the H atom is instead bound to a position on the ligand are also plausible scenarios.[89,90]
(27) Solis, B. H.; Hammes-Schiffer, S. *J. Am. Chem. Soc.* **2011**, *133*, 19036−19039.
(28) Sun, Y.; Bigi, J. P.; Piro, N. A.; Tang, M. L.; Long, J. R.; Chang, C. J. *J. Am. Chem. Soc.* **2011**, *133*, 9212−9215.
(29) Kilgore, U. J.; Stewart, M. P.; Helm, M. L.; Dougherty, W. G.; Kassel, W. S.; DuBois, M. R.; DuBois, D. L.; Bullock, R. M. *Inorg. Chem.* **2011**, *50*, 10908−10918.
(30) Razavet, M.; Artero, V.; Fontecave, M. *Inorg. Chem.* **2005**, *44*, 4786−4795.
(31) Wakerley, D. W.; Reisner, E. *Phys. Chem. Chem. Phys.* **2014**, *16*, 5739−5746.
(32) Kilgore, U. J.; Roberts, J. A. S.; Pool, D. H.; Appel, A. M.; Stewart, M. P.; DuBois, M. R.; Dougherty, W. G.; Kassel, W. S.; Bullock, R. M.; DuBois, D. L. *J. Am. Chem. Soc.* **2011**, *133*, 5861−5872.
(33) (a) Wiedner, E. S.; Roberts, J. A. S.; Dougherty, W. G.; Kassel, W. S.; DuBois, D. L.; Bullock, R. M. *Inorg. Chem.* **2013**, *52*, 9975−9988. (b) Wiedner, E. S.; Appel, A. M.; DuBois, D. L.; Bullock, R. M. *Inorg. Chem.* **2013**, *52*, 14391−14403.
(34) Fourmond, V.; Jacques, P.-A.; Fontecave, M.; Artero, V. *Inorg. Chem.* **2010**, *49*, 10338−10347.
(35) McCrory, C. C. L.; Uyeda, C.; Peters, J. C. *J. Am. Chem. Soc.* **2012**, *134*, 3164−3170.

DOI: 10.1021/acscatal.6b01387
ACS Catal. 2016, 6, 6114−6123

(36) Bhattacharjee, D.; Andreiadis, E. S.; Chavarot-Kerlidou, M.; Fontecave, M.; Field, M. J.; Artero, V. *Chem. - Eur. J.* **2013**, *19*, 15166−15174.
(37) Gerli, A.; Sabat, M.; Marzilli, L. G. *J. Am. Chem. Soc.* **1992**, *114*, 6711−6718.
(38) Manby, F. R.; Stella, M.; Goodpaster, J. D.; Miller, T. F. *J. Chem. Theory Comput.* **2012**, *8*, 2564−2568.
(39) Goodpaster, J. D.; Barnes, T. A.; Manby, F. R.; Miller, T. F. *J. Chem. Phys.* **2014**, *140*, 18A507.
(40) Solis, B. H.; Hammes-Schiffer, S. *Inorg. Chem.* **2011**, *50*, 11252−11262.
(41) Cramer, C. J.; Truhlar, D. G. *Phys. Chem. Chem. Phys.* **2009**, *11*, 10757−10816.
(42) Barden, C. J.; Rienstra-Kiracofe, J. C.; Schaefer, H. F. *J. Chem. Phys.* **2000**, *113*, 690−700.
(43) Diedrich, C.; Lüchow, A.; Grimme, S. *J. Chem. Phys.* **2005**, *122*, 021101.
(44) Jensen, K. P.; Roos, B. O.; Ryde, U. *J. Chem. Phys.* **2007**, *126*, 014103.
(45) Goel, S.; Masunov, A. E. *J. Chem. Phys.* **2008**, *129*, 214302.
(46) Barnes, T. A.; Goodpaster, J. D.; Manby, F. R.; Miller, T. F. *J. Chem. Phys.* **2013**, *139*, 024103.
(47) Werner, H.-J.; Knowles, P. J.; Knizia, G.; Manby, F. R.; Schütz, M.; Celani, P.; Korona, T.; Lindh, R.; Mitrushenkov, A.; Rauhut, G.; Shamasundar, K. R.; Adler, T. B.; Amos, R. D.; Bernhardsson, A.; Berning, A.; Cooper, D. L.; Deegan, M. J. O.; Dobbyn, A. J.; Eckert, F.; Goll, E.; Hampel, C.; Hesselmann, A.; Hetzer, G.; Hrenar, T.; Jansen, G.; Köppl, C.; Liu, Y.; Lloyd, A. W.; Mata, R. A.; May, A. J.; McNicholas, S. J.; Meyer, W.; Mura, M. E.; Nicklass, A.; O'Neill, D. P.; Palmieri, P.; Peng, D.; Pflüger, K.; Pitzer, R.; Reiher, M.; Shiozaki, T.; Stoll, H.; Stone, A. J.; Tarroni, R.; Thorsteinsson, T.; Wang, M. *MOLPRO, version 2012.1, a package of ab initio programs*, 2012; see www.molpro.net.
(48) Becke, A. D. *J. Chem. Phys.* **1993**, *98*, 5648−5652.
(49) Perdew, J. P. *Phys. Rev. B: Condens. Matter Mater. Phys.* **1986**, *33*, 8822−8824.
(50) Becke, A. D. *Phys. Rev. A: At., Mol., Opt. Phys.* **1988**, *38*, 3098−3100.
(51) Dunning, T. H. *J. Chem. Phys.* **1989**, *90*, 1007−1023.
(52) Pipek, J.; Mezey, P. G. *J. Chem. Phys.* **1989**, *90*, 4916−4926.
(53) Jiang, W.; DeYonker, N. J.; Wilson, A. K. *J. Chem. Theory Comput.* **2012**, *8*, 460−468.
(54) Yang, J.; Chan, G. K.-L.; Manby, F. R.; Schütz, M.; Werner, H.-J. *J. Chem. Phys.* **2012**, *136*, 144105.
(55) Riplinger, C.; Sampson, M. D.; Ritzmann, A. M.; Kubiak, C. P.; Carter, E. A. *J. Am. Chem. Soc.* **2014**, *136*, 16285−16298.
(56) (a) Boughton, J. W.; Pulay, P. *J. Comput. Chem.* **1993**, *14*, 736−740. (b) Hampel, C.; Werner, H.-J. *J. Chem. Phys.* **1996**, *104*, 6286−6297.
(57) (a) Schütz, M.; Manby, F. R. *Phys. Chem. Chem. Phys.* **2003**, *5*, 3349−3358. (b) Werner, H.-J.; Schütz, M. *J. Chem. Phys.* **2011**, *135*, 144116.
(58) (a) Schütz, M.; Werner, H.-J. *Chem. Phys. Lett.* **2000**, *318*, 370−378. (b) Schütz, M. *J. Chem. Phys.* **2000**, *113*, 9986−10001.
(59) (a) Kelly, C. P.; Cramer, C. J.; Truhlar, D. G. *J. Phys. Chem. B* **2007**, *111*, 408−422. (b) Lim, C.; Bashford, D.; Karplus, M. *J. Phys. Chem.* **1991**, *95*, 5610−5620.
(60) (a) Barone, V.; Cossi, M. *J. Phys. Chem. A* **1998**, *102*, 1995−2001. (b) Cossi, M.; Rega, N.; Scalmani, G.; Barone, V. *J. Comput. Chem.* **2003**, *24*, 669−681.
(61) Solis, B. H.; Hammes-Schiffer, S. *J. Am. Chem. Soc.* **2012**, *134*, 15253−15256.
(62) Solis, B. H.; Yu, Y.; Hammes-Schiffer, S. *Inorg. Chem.* **2013**, *52*, 6994−6999.
(63) Bondi, A. *J. Phys. Chem.* **1964**, *68*, 441−451.
(64) Floris, F.; Tomasi, J. *J. Comput. Chem.* **1989**, *10*, 616−627.
(65) Floris, F. M.; Tomasi, J.; Ahuir, J. L. P. *J. Comput. Chem.* **1991**, *12*, 784−791.
(66) Pierotti, R. A. *Chem. Rev.* **1976**, *76*, 717−726.
(67) Baffert, C.; Artero, V.; Fontecave, M. *Inorg. Chem.* **2007**, *46*, 1817−1824.
(68) Frisch, M. J.; Trucks, G. W.; Schlegel, H. B.; Scuseria, G. E.; Robb, M. A.; Cheeseman, J. R.; Scalmani, G.; Barone, V.; Mennucci, B.; Petersson, G. A.; Nakatsuji, H.; Caricato, M.; Li, X.; Hratchian, H. P.; Izmaylov, A. F.; Bloino, J.; Zheng, G.; Sonnenberg, J. L.; Hada, M.; Ehara, M.; Toyota, K.; Fukuda, R.; Hasegawa, J.; Ishida, M.; Nakajima, T.; Honda, Y.; Kitao, O.; Nakai, H.; Vreven, T.; Montgomery, J. A., Jr.; Peralta, J. E.; Ogliaro, F.; Bearpark, M.; Heyd, J. J.; Brothers, E.; Kudin, K. N.; Staroverov, V. N.; Kobayashi, R.; Normand, J.; Raghavachari, K.; Rendell, A.; Burant, J. C.; Iyengar, S. S.; Tomasi, J.; Cossi, M.; Rega, N.; Millam, J. M.; Klene, M.; Knox, J. E.; Cross, J. B.; Bakken, V.; Adamo, C.; Jaramillo, J.; Gomperts, R.; Stratmann, R. E.; Yazyev, O.; Austin, A. J.; Cammi, R.; Pomelli, C.; Ochterski, J. W.; Martin, R. L.; Morokuma, K.; Zakrzewski, V. G.; Voth, G. A.; Salvador, P.; Dannenberg, J. J.; Dapprich, S.; Daniels, A. D.; Farkas, O.; Foresman, J. B.; Ortiz, J. V.; Cioslowski, J.; Fox, D. J. *Gaussian09*; Gaussian Inc., Wallingford, CT, 2009.
(69) Niklas, J.; Mardis, K. L.; Rakhimov, R. R.; Mulfort, K. L.; Tiede, D. M.; Poluektov, O. G. *J. Phys. Chem. B* **2012**, *116*, 2943−2957.
(70) Peng, C.; Ayala, P.; Schlegel, H. B.; Frisch, M. J. *J. Comput. Chem.* **1996**, *17*, 49−56.
(71) Hratchian, H. P.; Schlegel, H. B. *J. Chem. Theory Comput.* **2005**, *1*, 61−69.
(72) Henkelman, G.; Uberuaga, B.; Jónsson, H. *J. Chem. Phys.* **2000**, *113*, 9901−9904.
(73) *CP2K*, 2015; http://www.cp2k.org.
(74) VandeVondele, J.; Krack, M.; Mohamed, F.; Parrinello, M.; Chassaing, T.; Hutter, J. *Comput. Phys. Commun.* **2005**, *167*, 103−128.
(75) Goedecker, S.; Teter, M.; Hutter, J. *Phys. Rev. B: Condens. Matter Mater. Phys.* **1996**, *54*, 1703−1710.
(76) Martyna, G. J.; Tuckerman, M. E. *J. Chem. Phys.* **1999**, *110*, 2810−2821.
(77) Grimme, S.; Ehrlich, S.; Goerigk, L. *J. Comput. Chem.* **2011**, *32*, 1456−1465.
(78) Solis, B. H.; Maher, A. G.; Honda, T.; Powers, D. C.; Nocera, D. G.; Hammes-Schiffer, S. *ACS Catal.* **2014**, *4*, 4516−4526.
(79) Harshan, A. K.; Solis, B. H.; Winkler, J. R.; Gray, H. B.; Hammes-Schiffer, S. *Inorg. Chem.* **2016**, *55*, 2934−2940.
(80) (a) Kaljurand, I.; Rodima, T.; Leito, I.; Koppel, I. A.; Schwesinger, R. *J. Org. Chem.* **2000**, *65*, 6202−6208. (b) Kaljurand, I.; Kütt, A.; Sooväli, L.; Rodima, T.; Mäemets, V.; Leito, I.; Koppel, I. A. *J. Org. Chem.* **2005**, *70*, 1019−1028.
(81) Hansch, C.; Leo, A. *Substituent Constants for Correlation Analysis in Chemistry and Biology*, 3rd ed.; Wiley-Interscience: New York, 1979.
(82) $Co^{IV}(H)$ is calculated to be 60 kcal/mol higher than $Co^{II}(NH)$ at the B3P86/6-311+G(d,p) level of theory.
(83) Marinescu, S. C.; Winkler, J. R.; Gray, H. B. *Proc. Natl. Acad. Sci. U. S. A.* **2012**, *109*, 15127−15131.
(84) Lee, C. H.; Dogutan, D. K.; Nocera, D. G. *J. Am. Chem. Soc.* **2011**, *133*, 8775−8777.
(85) Graham, D. J.; Nocera, D. G. *Organometallics* **2014**, *33*, 4994−5001.
(86) Solis, B. H.; Maher, A. G.; Honda, T.; Powers, D. C.; Nocera, D. G.; Hammes-Schiffer, S. *ACS Catal.* **2014**, *4*, 4516−4526.
(87) Solis, B. H.; Maher, A. G.; Dogutan, D. K.; Nocera, D. G.; Hammes-Schiffer, S. *Proc. Natl. Acad. Sci. U. S. A.* **2016**, *113*, 485−492.
(88) Fernandez, L. E.; Horvath, S.; Hammes-Schiffer, S. *J. Phys. Chem. Lett.* **2013**, *4*, 542−546.
(89) Lacy, D.; Roberts, G. M.; Peters, J. C. *J. Am. Chem. Soc.* **2015**, *137*, 4860−4864.
(90) Estes, D. P.; Grills, D. G.; Norton, J. R. *J. Am. Chem. Soc.* **2014**, *136*, 17362−17365.

DOI: 10.1021/acscatal.6b01387
ACS Catal. 2016, 6, 6114−6123